Article

Updating the sub-nanometric cognition of reconstructed oxyhydroxide active phase for water oxidation

Yu Sun[1,2,3,4], Yong Xie[1,2,4], Xiaoxuan Chen[1,2], Jing Wu[1,2], Pengfei Liu[1,2], Xin Wang[1,2,3], Zhen Tian[1,2], Wenhao Zheng[1,2], Zhouyu Jiang[1,2], Zhuo Kang [1,2] ✉ & Yue Zhang [1,2,3] ✉

Unveiling structure-activity correlations at the sub-nanoscale remains an essential challenge in catalysis science. During electrocatalysis, dynamic structural evolution drives the ambiguous entanglement of crystals and electrons degrees of freedom that obscure the activity origin. Here, we track the structural evolution of Ni-based model pre-catalysts ($Ni(OH)_2$, NiS_2, $NiSe_2$, NiTe), detailing their catalytically active state during water oxidation via operando techniques and theoretical calculations. We reveal the sub-nanometric structural difference of NiO_6 unit with a regular distortion in the reconstructed active phase NiOOH, codetermined by the geometric (bond lengths) and electronic (covalency) structure of the pre-catalysts on both spatial and temporal scales. The symmetry-broken active units induce the delicate balance of the p and d orbitals in NiOOH, further steering the modulation of catalytic intermediate configurations and mechanisms, with improved performance. This work recognizes the fine structural differences of the active phases from the sub-nanometer scale, and quantitatively explains their influence on activity. Our findings provide a more intuitive design framework for high-efficiency materials through targeted symmetry engineering of active units.

Catalytic materials are the workhorses of clean energy conversion and carbon reduction, facilitating the conversion of small molecules (H_2O, CO_2, N_2) into renewable fuels or chemical feedstocks (H_2, hydrocarbons, NH_3)[1–3]. However, the practical implementation of these processes remains constrained by the substantial energy barriers inherent to the anodic oxygen evolution reaction, particularly its demanding four-electron transfer kinetics[4]. Transition metal-based materials are attractive due to sustainable and economic considerations[2,5]. Generally, active units, which are the primary cornerstone of catalytic materials (e.g., MO_6 and MO_4 in spinel, MO_6 in perovskite, M for metallic elements), allow for the construction of diversified crystal structures as well as unique surface electronic states through corner/edge-sharing stacking[6,7]. Rational engineering of these units' symmetry and coordination environments therefore presents a critical route toward developing efficient, stable materials for carbon-neutral technologies[8–11].

The oxygen evolution reaction (OER) mechanism is intrinsically linked to the electronic structure of catalytic materials, particularly the

[1]Academy for Advanced Interdisciplinary Science and Technology, Beijing Key Laboratory for Advanced Energy Materials and Technologies, State Key Laboratory for Advanced Metals and Materials, University of Science and Technology Beijing, Beijing, PR China. [2]School of Materials Science and Engineering, Key Laboratory of Advanced Materials and Devices for Post-Moore Chips Ministry of Education, University of Science and Technology Beijing, Beijing, PR China. [3]School of Materials Science and Engineering, Peking University, Beijing, PR China. [4]These authors contributed equally: Yu Sun, Yong Xie. ✉e-mail: zhuokang@ustb.edu.cn; yuezhang@ustb.edu.cn

frontier molecular orbital characteristics and metal-ligand bonding interactions[12,13]. These properties are modulated by the configurational state or local symmetry of the active unit[14–20], where symmetry-breaking distortions create charge density gradients and localized fields that selectively stabilize catalytic intermediates[4,13,16–18], thereby circumventing adsorbate scaling relation limitations[20,21]. Current material design strategies leverage component engineering[22,23] and strain modulation[24] to systematically control these symmetry effects[25,26], with demonstrated correlations between unit symmetry and catalytic activity[8,13,16,19,24,26].

Despite these advances, fundamental challenges persist due to the dynamic nature of catalytic systems. Under operational conditions, catalytic materials are frequently subject to complex structural evolution including chemical bond/surface atomic oscillations, configurational evolution, and phase transition of the bulk[27–33]. Pioneering studies have also enlightened researchers to recognize that transition metal-based materials undergo dynamic evolution in water electrolysis in terms of comprehensive information on crystal structure, valence, coordination environment, morphology, etc.[5,6,10,27,33]. This will inevitably trap the catalytic materials in intricate interplay between structural and electronic degrees of freedom, complicating the identification of the configuration and symmetry of the true active units. More recently, it has been further demonstrated that the whole range of transition metal-based oxides, sulfides, phosphides, and other materials, relying on different crystalline forms such as spinel, perovskite, rock salt, etc., evolve into oxyhydroxide active species during OER with unified active units MO_6, supported by operando X-ray absorption fine structure, Infrared spectroscopy, Mössbauer spectroscopy, and other techniques[1,5,6,20,28,29,34,35].

Intriguingly, reconstructed oxyhydroxides with identical cationic compositions exhibit significant activity variations despite their structural and chemical similarities, implying potential subtle structural differentials that have been overlooked. In recent fragmented reports, some attempts from varied perspectives, like the synergy of interfacial reaction structures constituted from surface NiOOH and precatalytic matrix[36], the coordination environment of oxyanions-doped NiOOH[37,38], and the e_g band behavior of the distorted interfacial NiO_6 octahedron originated from active phase[5,13,20], have been proposed and analyzed to interpret the activity variances. However, the atomic-level intrinsic lattice discrepancy of reconstructed NiOOH in confined nano-interfaces from various pre-catalysts, as well as the associated evolution of the redox mechanism, remains unexplored. To uncover the underlying incentive, we quantitatively probe the fine structural differences in the reconstructed structures and update the diversity of the homologous cationic oxyhydroxides active phase that is traditionally recognized as unified, as well as the neglected differential of correlated catalytic paths, from the configuration and symmetry of active units at the sub-nanometer scale. This is expected to guide researchers in the precise exploration of efficient materials at confined interfaces by properly engineering the symmetry of active units in an organized and dynamic approach.

In light of this, a series of nickel-based compounds, including Ni(OH)$_2$, NiS$_2$, NiSe$_2$, and NiTe have been adopted as model materials, and their structural evolution as well as the symmetry of the active units in the reconstruction-terminated structures were systematically investigated via operando techniques. The results show that the reconstructed NiO_6 active units present sub-nanometer structural differentials, governed by pre-catalysts-dependent bond lengths and electronic covalency. The local charge changes of such reconstructed NiO_6 with sub-nanometric distortion polarize the catalytic intermediate state, with catalytic paths diverging from adsorbate evolution mechanism (AEM) to oxide path mechanism (OPM) and lattice-oxygen-mediated mechanism (LOM), and the NiOOH formed from NiS$_2$ presents superior activity (Fig. 1). This work experimentally demonstrates the fine-structured differential in active units for reconstructed structures at the sub-nanoscale, which is instrumental in cognizing the activity variance of reconstructed active phase from different pre-catalysts with homologous cations.

Results
Structural characterization of pre-catalysts
Nickel-based compounds (β-Ni(OH)$_2$, NiS$_2$, NiSe$_2$, NiTe) exhibit various crystal structures determined by metal-anion coordination configuration and stoichiometric ratios. Pyrite-type NiS$_2$ was achieved by hydrothermal treatment of as-synthesized β-Ni(OH)$_2$ nanosheets with thioacetamide at 180 °C, while NiSe$_2$ and NiTe were obtained analogously using selenium/tellurium precursors (Supplementary Fig. 1, Methods). Powder X-ray diffraction (XRD) confirms their respective space groups as P-3m1 (Ni(OH)$_2$), Pa-3 (NiS$_2$, NiSe$_2$), and P63/mmc (NiTe) (Supplementary Figs. 2–5a). X-ray absorption near-edge structure (XANES) analysis reveals a consistent Ni^{2+} oxidation state across all pre-catalysts (Fig. 2a left, Supplementary Fig. 6, and Supplementary Table 1)[39], matching theoretical predictions for thermodynamic stability. Fourier-transformed (FT) extended X-ray fine structure (EXAFS) quantify bond-length variations: Ni–O (2.07 ± 0.01 Å) in Ni(OH)$_2$ progressively elongates to Ni–S (2.38 ± 0.01 Å), Ni–Se (2.47 ± 0.01 Å), and Ni–Te (2.58 ± 0.01 Å) bonds (Fig. 2a right, Supplementary Fig. 7 and Supplementary Table 2)[40]. The NiX$_6$ octahedra in these nickel-based pre-catalysts (X = O, S, Se, and Te) adopt unique packing geometries, generating the regular discrepancy of Ni–X and Ni–Ni bond lengths in the lattices (Fig. 2b and Supplementary Fig. 8a). This might endow different atomic architectures and electronic structures, and further leave a discerned consequence on the surface reconstruction processes as well as the configurational state of the epitaxially reconstructed structural units in the confined nano-space, dependent on different crystal structures.

Morphology and elemental distribution characterization were also used to verify the alterations in the crystalline properties of the synthesized materials. In transmission electron microscopy (TEM) and atomic force microscopy (AFM) images (Supplementary Fig. 2d, e), a close-up inspection of Ni(OH)$_2$ reveals nanosheet structures whose thickness uniformly distributes between 5 and 10 nm. High-resolution TEM (HRTEM) images (Fig. 2c and Supplementary Figs. 2–5b) display clear lattice fringes with an interplanar spacing of 2.71 Å, 2.53 Å, 3.44 Å, and 1.97 Å, indexed to the (100), (210), (111), and (110) planes of Ni(OH)$_2$, NiS$_2$, NiSe$_2$, and NiTe, respectively, supported by the single-crystal-like diffraction spots from the selected-area electron diffraction pattern (Insets in Supplementary Figs. 2–5b). Energy dispersive X-ray spectrum (EDS) elemental mappings provide direct-viewing evidence for the uniform elemental distribution (Supplementary Figs. 2–5c), verifying phase purity.

To further investigate the evolution of electronic structure for these nickel-based compounds with anion substitution, density functional theory (DFT) calculation was conducted (Supplementary Fig. 8b). The projected density of state (PDOS) results show that, with the continuous substitution of anionic ligand in Ni(OH)$_2$ by sulfur group elements, the p-band center in NiSe$_2$ is closest to the Fermi level, suggesting enhanced hydroxide adsorption capacity – a critical precursor to structural reconstruction[35]. In addition, the d–p orbital hybridization of the Ni–X bond increases (the difference of band center energy of d and p, ε_{d-p}, decreases from 1.16 eV to 0.75 eV) upon substitution of OH with S in Ni(OH)$_2$ to construct NiS$_2$, and this strengthening in orbital hybridization is more pronounced in NiSe$_2$ (ε_{d-p} 0.29 eV), whereas the hybridization of NiTe recedes slightly (0.98 eV for ε_{d-p}). The enlarged orbital hybridization means enhanced Ni–X covalency, which facilitates charge transfer and interactions at the surface of the material[1,5], may positively contribute to the subsequent chemical process.

These findings establish that anion substitutions might play a vital role in modulating the electronic environments of the metal Ni centers,
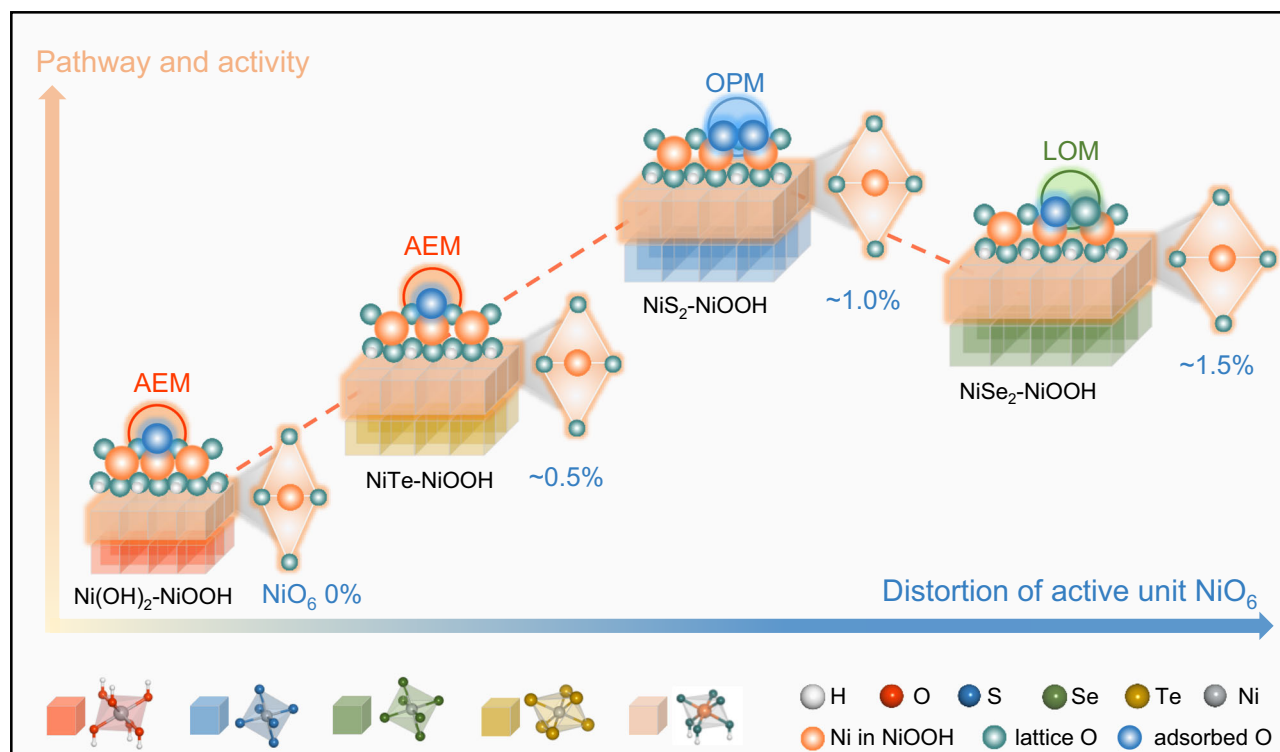
Fig. 1 | Schematic illustration. The structure-activity correlations of reconstructed oxyhydroxides in terms of the sub-nanometer scale structural differences of active unit NiO_6 configuration. The red, blue, green, and yellow cubes represent the matrix configurations NiX_6 forming the pre-catalyst, where X refers to OH, S, Se, and Te, respectively. For the surface reconstructed NiOOH (peach puff cube), the orange, teal, and light blue spheres represent Ni, lattice O, and adsorbed O atoms, respectively.

potentially promoting the structural flexibility for the ensuing reconstruction process, and resulting in the fine structural differences of reconstructed NiO_6 active unit in confined nano-interfaces during the service process. Detailed operando characterization results, confirmed by theoretical calculations, are discussed below.

Operando observation of the fine structural differentials of active unit NiO_6

To gain an in-depth understanding on the dynamic reconstruction process and the fine structural difference in the perspective of the configuration and symmetry of the terminated reconstruction units during the OER process, nickel-based precatalytic compounds were then investigated by operando electrochemical spectroscopies (for details see the Methods). Supplementary Figs. 9–12 present the operando XANES and the FT-EXAFS spectra in *R*-space of the samples recorded at open-circuit potential (OCP), 1.15 V, 1.35, 1.45, and 1.55 V versus reversible hydrogen electrode (vs. RHE). Critical analysis of Supplementary Figs. 9–12a reveals systematic higher energy shifts in Ni K-edge absorption energy across all materials with increasing applied potentials. Quantitative valence state analysis (Fig. 3a left and Supplementary Table 3) demonstrates final Ni oxidation states at 1.55 V (vs. RHE) of +3.82 for $Ni(OH)_2$-derived phases, contrasting with +3.42 (NiS_2), +3.34 ($NiSe_2$), and +3.73 ($NiTe$), confirming reconstruction-induced electronic structure modifications at nickel sites.

In the case of the local coordination environment, similar results are acquired from the FT-EXAFS spectra in *R*-space (Supplementary Figs. 9–12b). Compared with the profiles collected at OCP, the Ni–X bond peaks in these samples display a gradually declining trend from 1.35 V vs. RHE, indicative of structural transformation from precursor Ni–X_6 octahedra to reconstructed Ni–O configurations. Notably, spectral convergence toward γ-NiOOH references occurs at 1.55 V (vs. RHE) (Supplementary Fig. 13), with XANES linear combination fitting

confirming complete phase reconstruction (Supplementary Fig. 14, Supplementary Table 6). A detailed description of the restructuring into γ-NiOOH is directly identified from the material-phase structural point of view by further operando XRD fitting (Supplementary Figs. 15–19, Supplementary Table 7). More precisely fitting the EXAFS results (right axis in Fig. 3a, Supplementary Figs. 9–12c, and Supplementary Tables 4, 5), the Ni–X coordinate number (CN) of $Ni(OH)_2$ decreases from 6.0 ± 0.7 at OCP to 5.8 ± 0.6 at 1.35 V vs. RHE and 5.3 ± 0.5 at 1.55 V vs. RHE. For NiS_2, $NiSe_2$, and NiTe, the decline trend is evidently enhanced, culminating in 4.9 ± 0.6, 4.7 ± 0.7, and 5.0 ± 0.5 for Ni–O CN at 1.55 V vs. RHE, respectively.

The lower Ni–O CN designates that the reconstructed NiOOH accumulates more oxygen vacancies (Ov), which also implies that a variance in the state of the NiO_6 active unit, and the resulting Ov could produce extra electrons in the surrounding metal atoms, thus lowering the valence state of the metal atoms. The formation of oxygen vacancies in these pre-catalysts during the OER was confirmed by the electron paramagnetic resonance (EPR) measurement[41]. As shown in Supplementary Fig. 21, the quasi-operando EPR spectra of these pre-catalysts exhibit an obviously larger peak, which indicates Ov generation during the OER. Post-reaction structural analyses (Details see Supplementary Figs. 22–26, Supplementary Table 8) confirm vacancy persistence in catalytically active configurations. The contrasting results suggest that the concentration of Ov in different materials augments with the increasing potential during service, and more oxygen vacancies can be created with the further substitution of the elements S and Se in those Ni-based precatalytic compounds, which is in conformity with the results of the CN fitted by XAFS.

Extended edge fitting results at 1.55 V reveals the concrete structural difference of the reconstructed NiOOH species originated from the above-mentioned pristine materials. Explicitly, the Ni–Ni bond length of the reconstructed Ni oxyhydroxide derived from $Ni(OH)_2$
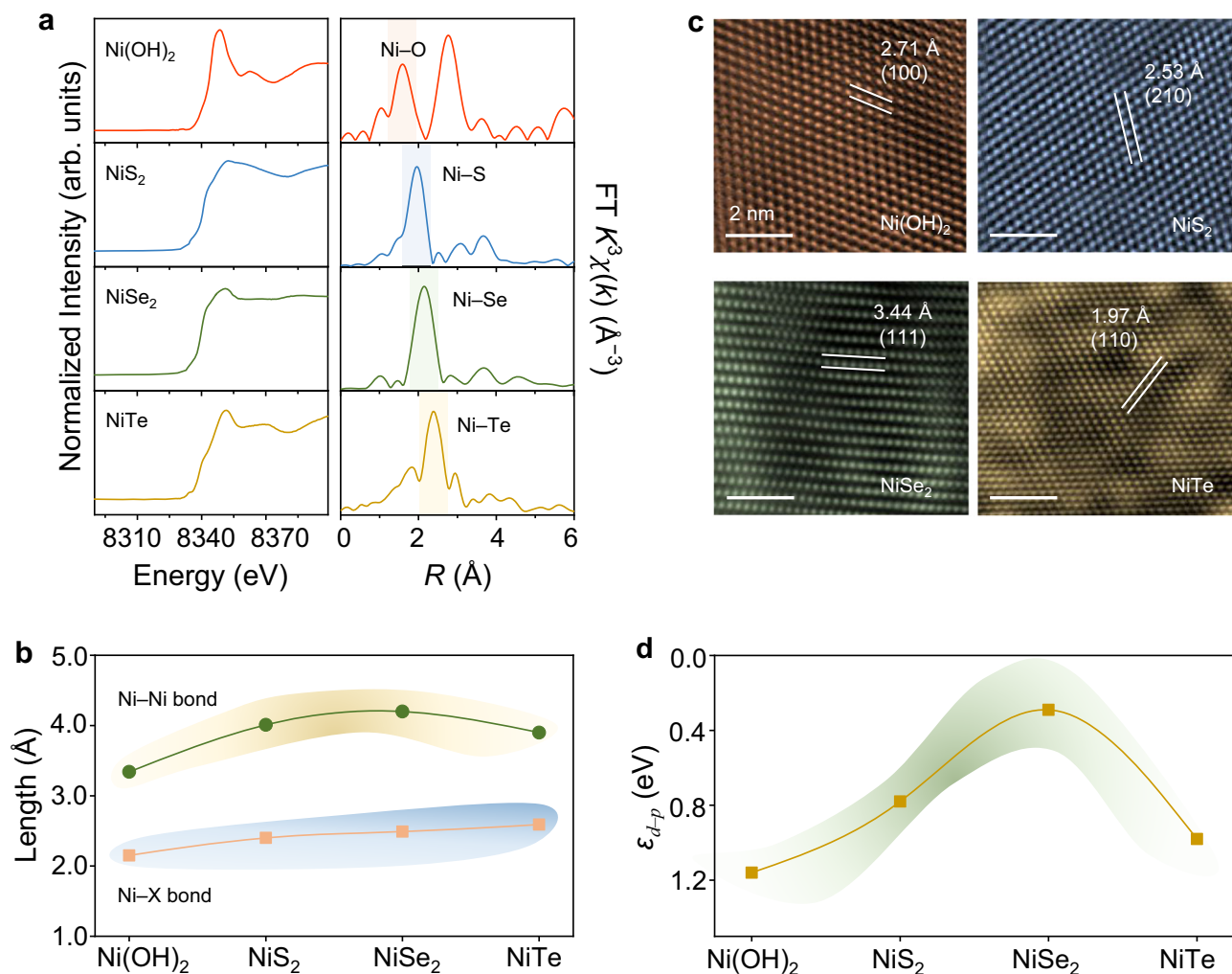
Fig. 2 | Structural characterizations of nickel-based pre-catalysts. a Normalized Ni K-edge XANES analysis (left axis) of samples (Ni(OH)$_2$, NiS$_2$, NiSe$_2$, NiTe), as well as the corresponding k^3-weighted Fourier transform (FT) Ni K-edge EXAFS spectra (right axis). **b** Calculated Ni–X/Ni–Ni bond length of Ni(OH)$_2$, NiS$_2$, NiSe$_2$, and NiTe.

c High-resolution TEM image of samples. Scale bars, 2 nm. **d** Calculated d–p band center energy difference (ε_{d-p}) of the nickel-based compounds. Source data are provided as a Source Data file.

(Ni(OH)$_2$-NiOOH) is $2.81 \pm 0.01\,\text{Å}$, and this value further varies to $2.84 \pm 0.01\,\text{Å}$, $2.85 \pm 0.01\,\text{Å}$, and $2.82 \pm 0.01\,\text{Å}$ for the NiS$_2$, NiSe$_2$, and NiTe reconstructed Ni oxyhydroxide materials (denoted as NiS$_2$-NiOOH, NiSe$_2$-NiOOH, NiTe-NiOOH), respectively (Fig. 3b, Supplementary Tables 4 and 5). Corresponding Ni–O bond length analysis shows analogous distortion patterns, and the refined distortion extent of the reconstruction-induced NiO$_6$ unit are 1% (NiS$_2$-NiOOH), 1.5% (NiSe$_2$-NiOOH), and 0.5% (NiTe-NiOOH), respectively, in comparison with that of Ni(OH)$_2$-NiOOH (Fig. 3c). XRD Rietveld refinement validates these fine structure differences in the reconstructed phase γ-NiOOH (Supplementary Fig. 20). These results suggest that the sub-nanometric structural differentials of the NiO$_6$ active units in the terminated structure NiOOH. The structural inheritance of reconstructed active phases derives from pre-catalyst-dependent lattice architectures, whereby elongated Ni–X/Ni–Ni bond lengths in pristine materials amplify interfacial lattice mismatch during epitaxial reconstruction. This mismatch propagates sub-nanometric structural distortions in surface-confined NiOOH units on the spatial scale through strain accumulation.

Furthermore, enhanced electron transfer capacity for the pristine materials also improves the ability for anion oxidation/leaching to facilitate the reconstruction process. Concomitantly, this may lead to the breakage of massive Ni–X bonds in the pre-catalysts during the

OER process, as well as the creation of more oxygen vacancies due to the untimely bonding of OH or O with Ni, and ultimately induces distortions of the geometrical configuration of the reconstructed NiO$_6$ unit on the temporal scale. This dynamic symmetry modulation is substantiated by time-resolved anion leaching kinetics and nickel oxidation currents (Supplementary Fig. 27), supported by XAFS/EPR-derived Ni valence, coordination, and Ov evolution. NiS$_2$ and NiSe$_2$ possess extended Ni–Ni and Ni–X bonds than the Ni(OH)$_2$ structure (for specific data, see Fig. 2a and Supplementary Table 2), and their covalency becomes further stronger with substitution from S to Se, which would result in a continuum distortion of the active unit in NiOOH. For NiTe materials, the further reduction of the Ni–Ni bond length and electron transfer capacity in their structures (-3.95 Å for Ni–Ni bond, and 0.98 eV for ε_{d-p}), both of which together lead to less distortion of the generated active structures, substantiated by the Te elemental loss rate.

Operando Raman results (Fig. 3d and Supplementary Fig. 28) provide further verification of the fine structural differences of reconstructed NiOOH. The two characteristic peaks (i.e., in-plane vibrational peak $\delta_{\text{Ni-O}}$ and out-of-plane vibrational peak $\nu_{\text{Ni-O}}$)[42,43] of NiOOH gradually become clarified along with the precursor signal attenuation as the applied potentials increase. Comparative analysis at 1.6 V (vs. RHE) demonstrates systematic $\delta_{\text{Ni-O}}$ redshift between the
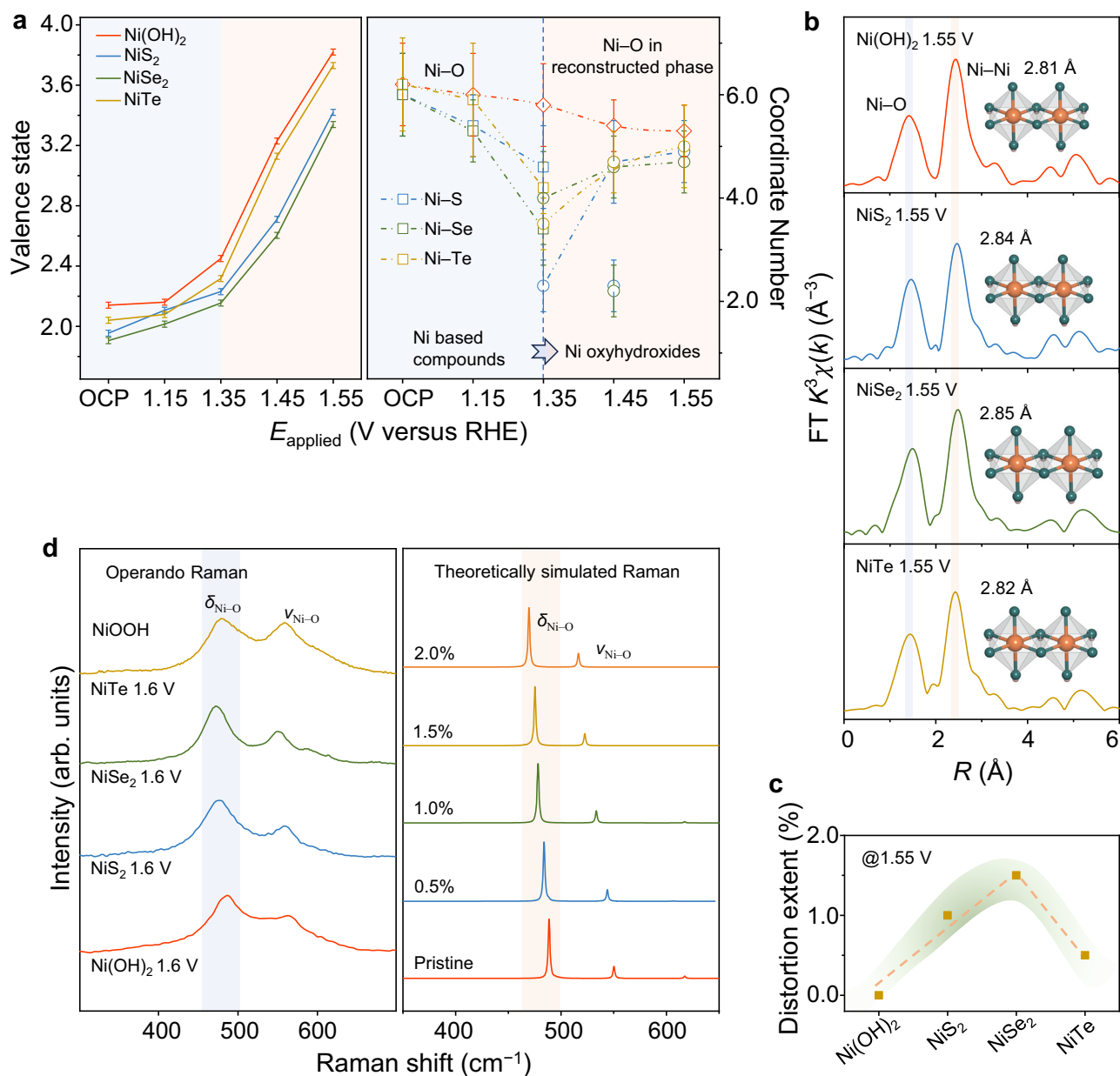
Fig. 3 | Operando identification of the subtle differentials of reconstructed active structures. a The average valence states of nickel element from operando XANES spectra for $Ni(OH)_2$, NiS_2, $NiSe_2$, NiTe (Left axis) at OCP, 1.15 V, 1.35, 1.45, and 1.55 V (vs. RHE). Error bars represent the standard deviation from at least three independent measurements. The right axis shows the changes in coordination number corresponding to the applied potentials. **b** The operando FT k^3-weighted Ni K-edge EXAFS at 1.55 V (vs. RHE). R denotes the interatomic distance; k is the photoelectron wave number. Inset is the corresponding NiO_6 active unit of reconstructed NiOOH from different pre-catalysts, confirming bond

reconstruction-derived NiOOH for $Ni(OH)_2$, NiS_2, $NiSe_2$, and NiTe, where the orange, teal, and light pink spheres represent Ni, O, and H atoms, respectively. **c** The concrete structural differences of the active unit in distortion extent of $Ni(OH)_2$, NiS_2, $NiSe_2$, NiTe at 1.55 V (vs. RHE). **d** Operando Raman spectra (Left axis) of $Ni(OH)_2$, NiS_2, $NiSe_2$, NiTe at 1.6 V (vs. RHE) and the theoretically simulated Raman spectra of NiOOH with the corresponding structural differences (Right axis). Source data are provided as a Source Data file.

elongation-induced lattice expansion. Specifically, the δ_{Ni-O} vibrational peak positions of NiOOH generated from NiS_2, $NiSe_2$, and NiTe deviate by $9.9 \pm 1\,cm^{-1}$, $12.9 \pm 1\,cm^{-1}$, and $5.3 \pm 1\,cm^{-1}$, respectively, to that of $Ni(OH)_2$-NiOOH (Fig. 3d left). These results experimentally prove that the reconstruction-induced active unit NiO_6 presents a regular distortion. Additionally, Raman simulations of theoretically constructed NiOOH structures with different distortion extents based on the above experimental results further identify the red-shift phenomenon and their mathematical values of the δ_{Ni-O} vibrational peak, and the results are also in general agreement with those of the operando XAFS (Fig. 3d right and Supplementary Tables 4 and 5).

Time-resolved operando XAFS and XRD further corroborate that the Ni-based pre-catalysts are essentially transformed into γ-NiOOH during OER, reaching an equilibrium state, and subsequently engaging in the actual catalysis. The results of more comprehensive XANES linear fittings (Supplementary Figs. 29–32 and Supplementary Tables 9, 10), EXAFS (Supplementary Figs. 33–36 and Supplementary Tables 11–14) and XRD (Supplementary Figs. 37–41 and Supplementary Table 15) fittings and refinements for the reconstructed system also demonstrate structural distortion patterns that are fundamentally in accordance with those in Fig. 3c. The geometric structure (Ni–X/Ni bond lengths) in pre-catalysts influences the epitaxially reconstructed phase on a spatial scale yielding massive atomic mismatches, while the

electronic structure (covalency) in pre-catalysts regulates the reconstruction on a temporal scale inevitably conferring active structure defects. Their interplay dynamically modulates the reconstructed NiO_6 symmetry and further dictate the sub-nanometric structure differences of NiOOH on account of the relaxation in the active unit linkages. Such fine structural differences in reconstructed active units may modify the electronic structure to further optimize the OER activity, and its clear structure-activity correlation is discussed in the subsequent subsection.

Insight into the structure-activity correlations at the sub-nanoscale

To systematically investigate the effect of sub-nanometer structural differentials on the catalytic activity, we conducted comprehensive electrochemical characterization of reconstruction-induced nickel-based pre-catalysts under alkaline conditions (see Methods). As mentioned above, the pre-catalysts are wholly transformed into NiOOH species with different distortion extents during the oxidation service, and function as actual catalysts for the OER thereafter. It is noteworthy that we pretreated the nickel-based pre-catalysts coated on carbon paper under 10 mA cm^{-2} with the chronopotentiometric technique for 2 h prior to electrochemical analysis (Supplementary Fig. 42). The complete conversion of these pre-catalysts to active structure of Ni-oxyhydroxide has been confirmed by the results of soft X-ray adsorption spectroscopy (Supplementary Fig. 43), X-ray photoelectron spectroscopy (Supplementary Figs. 44, 45), and TEM (Supplementary Figs. 46–49). Steady-state linear scanning voltammetry (LSV) in Ar-saturated 1 M KOH indicates that Ni(OH)$_2$-NiOOH displays an overpotential of 407 mV at a current density of 10 mA cm^{-2}. With the consecutive substitution of sulfur group elements in the pre-catalysts, the corresponding overpotentials at 10 mA cm^{-2} of NiS$_2$-NiOOH and NiSe$_2$-NiOOH continue to decrease to 218 mV and 249 mV, and then it bounces back for NiTe-NiOOH (Fig. 4a, Supplementary Fig. 50a). The Tafel slope, as a pivotal kinetic parameter, is usually used to investigate the rate-determining step of an electrochemical process[44]. Here, compared with 126.4 mV dec^{-1} for the Ni(OH)$_2$-NiOOH, NiS$_2$-NiOOH performs superior properties over other catalysts, with the Tafel slope as low as 29.2 mV dec^{-1}, as shown in Fig. 4b, suggesting that Ni-oxyhydroxide with different distortion extents may effectively regulate the OER kinetic process and mechanisms.

The activity variance of these materials is in accordance with the electrochemical impedance spectroscopy results and the double-layer capacitance plot data. As shown in Supplementary Fig. 50b, Nyquist plots are fitted to a simplified Randles equivalent circuit model[45], and the charge-transfer resistance (R_{ct}) of NiOOH induced by NiS$_2$, NiSe$_2$, and NiTe measured at 270 mV overpotential decline considerably in comparison with that of Ni(OH)$_2$-NiOOH (R_{ct} is 60.64 Ω), and NiS$_2$-NiOOH shows the smallest R_{ct} value of 8.15 Ω. This result demonstrates that the appropriate structural distortion at sub-nanometer scale extraordinarily promotes the charge transfer, thus improving the reaction activity (Supplementary Fig. 50c). Notably, the double-layer capacitance (C_{dl}) results show roughly similar results, with only a small increase in C_{dl} (7.89, 9.26, 5.92 mF cm^{-2}) for NiOOH induced from NiS$_2$, NiSe$_2$, and NiTe compared to Ni(OH)$_2$-NiOOH (5.30 mF cm^{-2}), and further electrochemically active surface area (ECSA) normalized activity also exhibit an alike trend (Supplementary Figs. 51, 52). Moreover, the turnover frequency (TOF) and mass activity were also calculated to assess the intrinsic activity (Supplementary Fig. 50d and Table 16). Specifically, NiS$_2$-NiOOH delivers comparable TOF and mass activity of 0.1027 s^{-1} and 322.775 mA mg$_{metal}^{-1}$, respectively, at an overpotential of 270 mV in alkaline electrolyte, which is ~85.6-fold higher than that of Ni(OH)$_2$-NiOOH, and ~4.3-fold than that of RuO$_2$-OER catalysts. These metrics establish that activity enhancement originates from NiO_6 distortion rather than surface area variations.

DFT calculations were performed to investigate electronic structure variations in distorted NiOOH models (0%, 0.5%, 1%, 1.5%, and 2%, Supplementary Fig. 53). The corresponding PDOS and their band center energies (ε) are given in Fig. 4c (see Supplementary Table 17 for details). PDOS results reveal gradual electronic rearrangement due to the distortion of the active unit NiO_6 in the lattice, in which the O p and Ni d orbitals are both gradually raised with the increasing extent of distortion. This orbital realignment could establish a modified electronic equilibrium at the surface, potentially influencing intermediate adsorption configurations during OER.

The d orbitals, typically, split into an electron-filled lower Hubbard band (LHB) and an empty upper Hubbard band (UHB), due to d–d onsite Coulomb interactions (U), namely Mott Hubbard splitting[43]. Compared to pristine models, the volume of Ni d orbital in distorted structure is reduced, which attenuates the splitting of the d orbitals, and the corresponding U value is consequently reduced as well as the LHB partially shifts upwards (Fig. 4d, Supplementary Fig. 54a, and Supplementary Table 17). Further specific analysis of the $d_{x^2-y^2}$ with d_{z^2} orbital energy displays that distortion may decrease orbital splitting energies (Supplementary Fig. 54b, Supplementary Table 17)[23], a phenomenon that could enhance electron occupancy of e$_g$ orbitals and their energy levels elevation with possible implications for the oxygen-adsorbing intermediates on the surface. Here, we also quantitatively analyze the correlation between U and charge transfer energy (Δ) (Fig. 4d), where U is close to Δ in the pristine unit (overlapping of LHB and O p band), and electrons might be transferred metal-to-metal to a large extent in distinct active units; With further increase in the distortion extent of the NiO_6 (1% and 2%), O p-bands shift upward and Δ gradually diminishes and reaches $U > \Delta$ at 2% distortion, which would be beneficial to creating more oxygen vacancies, enabling the enhanced O p-band characters in the vicinity of the Fermi energy level, and permitting the electron transfer process to be carried out between the metal and the oxygen inside the active units (or the electrons could easily escape from the p-band of the ligand oxygen) during the catalytic reaction[13,19,20].

Comprehensive analysis of the theoretical calculations and the experimentally evaluated activity metrics illustrates (Fig. 4e, Supplementary Table 17) that the charge transfer energies of the catalytic materials are highly correlated with the OER activity (overpotential @10 mA cm^{-2}) as the configuration of the active unit NiO_6 continues to be distorted. Accordingly, the symmetry of the active unit might become a critical influence factor on the catalytic activity. Also, the modulation of the electronic state can be achieved by such configurational state tuning, which would further regulate the oxygen adsorption intermediates on the surface of the metal elements or activate the surface oxygen atoms to be involved in the catalytic process to implement the selective optimization of water oxidation.

This sustained structural distortion-induced electronic modulation constitutes the fundamental origin of activity differences among reconstructed oxyhydroxides. Notably, this also reveals an alternative strategy for material designing that combines self-reconfiguration with interfacial confinement. That is, maneuvering the phase reconstruction by synthetically adjusting the ligand behavior in pre-catalysts in confined nano-interfaces through the discrepancy of both geometric structure (affecting the terminated active phase on the spatial scale) and electronic structure (affecting the reconstruction process on the temporal scale) as a bridge to customize the symmetry of the actual catalytic active unit.

Influence of the sub-nanometric structural difference of reconstructed NiO_6 on OER mechanism

To explore the influence of NiO_6 structural differentials on OER mechanism, we performed DFT calculations across three distinct reaction pathways with a unified O–Ni–O–Ni–O active site configuration (Fig. 5a)[46–49]. The conventional adsorbate evolution mechanism
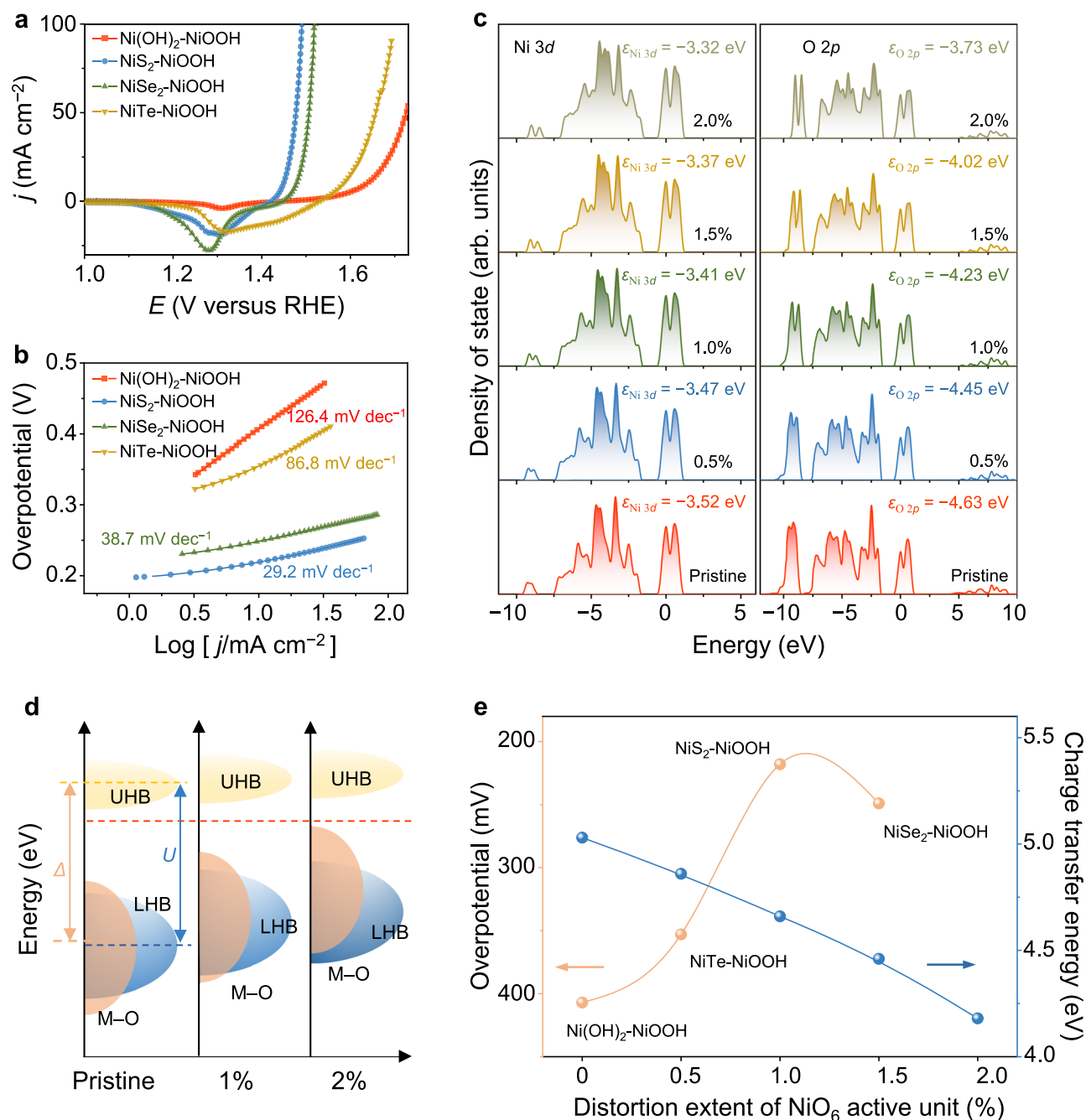
Fig. 4 | Evaluation of OER activity and electronic structure of active unit NiO_6 with different structural distortion. a OER polarization curves of Ni(OH)_2-NiOOH, NiS_2-NiOOH, NiSe_2-NiOOH, NiTe-NiOOH catalysts on carbon paper in Ar-saturated 1 M KOH at a scan rate of 5 mV s^{-1}. **b** Corresponding OER Tafel plots derived from the polarization curves. **c** Computed Ni 3d, O 2p PDOS of NiOOH with different distortion extents. **d** Schematic energy bands of different distorted NiOOH in consideration of Mott-Hubbard splitting. **e** Computed charge transfer energy related to the overpotentials (@10 mA cm^{-2}) of different distortion extents of NiO_6 active unit. Source data are provided as a Source Data file.

(AEM) involves sequential *OH, *O, and *OOH intermediate formation (* denotes the active site on the catalyst surface)[46,47], while the lattice-oxygen-mediated mechanism (LOM) comprises the engagement of activated lattice oxygen (O_L) in OER to facilitate *O–O_L coupling[48]. In the scenario of the oxide path mechanism (OPM), the metal sites in the adjacent active units NiO_6–NiO_6 at appropriate positions work cooperatively to promote water oxidation and trigger the coupling of the *O radicals to generate O_2 without the involvement of lattice oxygen in a low energy barrier[49].

For pristine NiOOH (Supplementary Fig. 55, Supplementary Table 18), the AEM scenario presents the lowest overpotential of

1.32 eV with *O formation as rate-determining step (RDS), outperforming LOM (RDS, 1.48 eV, *O-O_L coupling) and OPM (RDS, 1.72 eV, *O formation). In 1%-distorted NiOOH (NiS_2-NiOOH), OPM becomes preferential with reduced *O radical coupling barriers (RDS, 1.17 eV, Fig. 5b, Supplementary Fig. 57, Supplementary Table 20). It is noteworthy that the formation energy of *O in the OPM of the pristine NiOOH structure is very high ($\Delta G = 1.72$ eV), and the 0.5%-NiOOH structure exhibits essentially a parallel result (Supplementary Fig. 56, Supplementary Table 19), whereas there is a decrease for the energy of *O forming in the OPM path of the 1%-NiOOH structure ($\Delta G = 1.07$ eV), with the radical oxygen coupling as the RDS. This suggests that proper
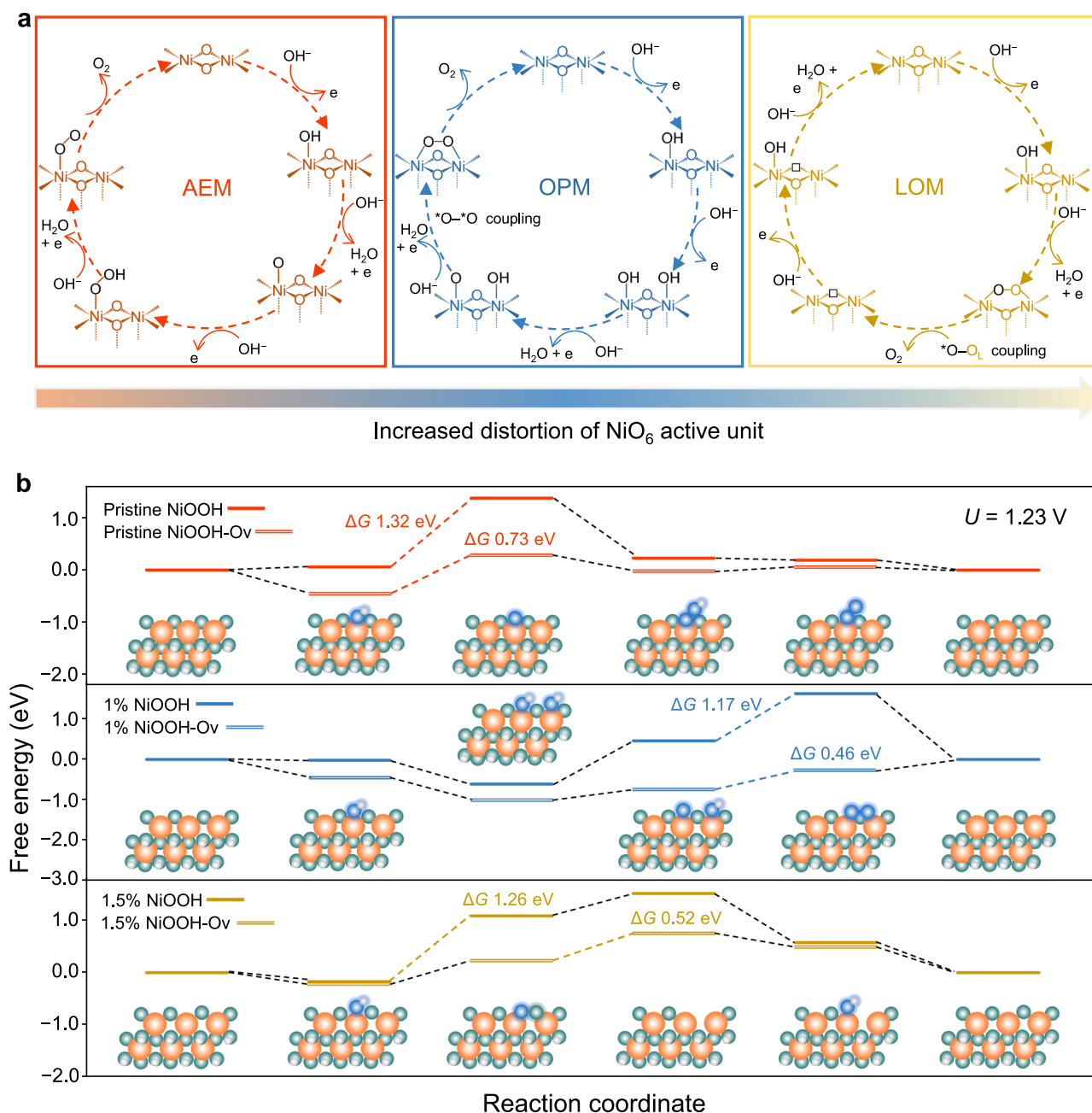
Fig. 5 | OER mechanism analysis based on DFT simulations. a OER mechanism of AEM, LOM, and OPM for NiOOH. The empty square represents the oxygen vacancy (Ov). *O and O_L stand for adsorbed oxygen and lattice oxygen, respectively. **b** Calculated OER free-energy diagrams at $U = 1.23$ V for pristine NiOOH, 1% distorted NiOOH, and 1.5% distorted NiOOH with and without oxygen vacancy. Insets are the schematic illustrations of catalytic intermediate configurations on the lattice without oxygen vacancy. The orange, teal, white, and light blue spheres represent Ni, O, H, and adsorbed O atoms, respectively. Source data are provided as a Source Data file.

configurational distortion might enhance the adsorption of *O and lead to a closer matching of the local electric field of the neighboring NiO_6-NiO_6 active units in the NiOOH structure, thereby optimizing the coupling of the adjacent *O radicals more smoothly and their subsequent desorption.

At 1.5% distortion ($NiSe_2$-NiOOH), as shown in Fig. 5b, Supplementary Fig. 58, and Supplementary Table 21, the potential barrier for the LOM reaches 1.26 eV (*O–O_L for the RDS step), which is lower than those of the AEM and OPM by 0.11 and 0.16 eV, respectively. Also, the oxygen coupling energies ($\Delta G = 1.26$ eV) in the LOM pathway of the 1.5%-NiOOH structure decrease by 0.22 eV and 0.1 eV in comparison with those in the LOM pathway of the pristine and 1%-distorted NiOOH

structures ($\Delta G = 1.48$ eV, $\Delta G = 1.36$ eV), respectively. This computational trend suggests LOM could become more accessible to 1.5%-NiOOH ($NiSe_2$-NiOOH) in the OER process than AEM and OPM, which is also in general agreement with the results of PDOS calculations on the oxygen properties near the Fermi energy level orbitals.

It has been demonstrated that the anionic behavior of precatalytic materials effectively regulates the reconstruction process and inevitably generates oxygen vacancies in the terminally active structure, distorting the active unit. As such, to further explore the effect of oxygen vacancies in the OER process, we also investigated the free energy of the four-electron OER process for the series of distorted NiOOH with oxygen vacancy (Fig. 5b, Supplementary Figs. 59–62,

Supplementary Tables 22–25). After the introduction of Ov, the results for NiOOH with different structural distortions basically match those without oxygen vacancies. More specifically, the calculated over-potentials of active structures containing vacancies in different extents of distortion are partially reduced in all three paths, with the over-potentials of the corresponding paths for the pristine NiOOH·Ov (AEM path) and the 1% distorted NiOOH·Ov (OPM path) being dropped by 0.59 eV and 0.7 eV, respectively. The presence of oxygen vacancies would provide adsorbed oxygen (*O) with a greater capacity to migrate and potentially fill the vacancies, i.e., *O bonded to two Ni exhibits superior adsorption stability compared to single-bonded adsorbed *O, potentially diminishing the energy depletion of the *OH to *O process. On the other hand, the formation of Ov in 1% and 1.5% distorted NiOOH further decrease the LOM pathway overpotential by 0.68 and 0.74 eV, respectively, which implies that Ov activates the oxygen atoms on the surface of highly distorted NiO_6 active unit under these computational conditions, rendering it more susceptible to participate in the oxygen coupling process and promoting the OER reaction.

To experimentally probe the OER mechanism, we employed operando Raman spectroscopy and resolved its oxygen adsorption intermediates during the OER reaction. For $Ni(OH)_2$-NiOOH and NiTe-NiOOH, Raman peaks at ~984 cm^{-1} and ~1065 cm^{-1} were observed, as shown in Fig. 6a. When the potential reaches the OER region (≥1.45 V), the peaks appear gradually and increases sharply in intensity with increasing applied voltage, which is attributed to the formation of abundant reactive intermediates, *OOH and adsorbed oxygen $*O_2$ at metal sites in the OER of the AEM path, as reported in the recent literature (refs. 3,35,47,50). For NiS_2-NiOOH, a distinct Raman peak was observed at 1076 cm^{-1}, ascribed to the formation of *O–*O bonds, suggesting oxygen bridges forming from two oxygen radicals between metal sites in the OER of the OPM pathway, and the associated peak at 1120 cm^{-1} is assigned to superoxide species (metal*–O–O), which are intermediates before the release of O_2[3,48,49,51]. This feature is consistent with the calculated OPM pathway where radical oxygen coupling is the rate-determining step. In contrast, the reaction intermediates of the $NiSe_2$-NiOOH material exhibited different results from those mentioned above, and a peak at 872 cm^{-1} was detected, which represents *OH intermediates[52] and suggests that the OER mechanism may be different from the above two pathways. Notably, both NiS_2-NiOOH and $NiSe_2$-NiOOH materials were also observed to present Raman peaks at ~984 cm^{-1} and ~1065 cm^{-1} (*OOH and $*O_2$ intermediates), which indicates that the catalytic materials might have a mutual competition of multiple reaction pathways during water oxidation, and further combining with the theoretical calculations, it can be noted that the dominant reaction mechanisms of those two may favor OPM and LOM, respectively.

Besides, operando differential electrochemical mass spectrometry (DEMS) with isotope labeling was conducted to confirm OER pathway assignments[3,35,53]. We designed a two-step DEMS experiment using $H_2^{18}O$ and $H_2^{16}O$ as support solutions (1 M KOH). In the first step, the reconstructed materials of the nickel-based precatalytic compounds mentioned above were coated on a porous gas-permeable gold working electrode and subjected to three CV cycles (1.1–1.7 V vs. RHE) in $H_2^{18}O$ electrolyte. The mass signals of the OER gas products recorded for the studied samples were illustrated in Supplementary Figs. 63 and 64. For OPM-type OER, $^{16}O_{ads}$ at adjacent Ni sites may couple together to form $^{32}O_2$. Figure 6b Left shows that $^{32}O_2$ is stably produced by NiS_2-NiOOH in each CV cycle. In comparison, the other compounds steadily produce $^{34}O_2$ and $^{36}O_2$, and the $^{32}O_2$ product signal could not be distinguished from the noise background. The next step is to clean the ^{18}O-labeled catalytic material with a large amount of $H_2^{16}O$ water, and then run it in the $H_2^{16}O$ electrolyte. Likewise, if OPM acts on the NiS_2-NiOOH, the remaining surface adsorbates (containing ^{18}O) would probably couple together to form the $^{36}O_2$ product, whereas $Ni(OH)_2$ and NiTe-induced NiOOH are not detected as any $^{36}O_2$

product. As shown in Fig. 6b right along with Supplementary Figs. 63 and 64, the DEMS results agree with our predictions. Considering the catalysts have similar surface areas, the effect of physically adsorbed $H_2^{18}O$ during OER can be excluded. Of note, $NiSe_2$-NiOOH yields a small amount of $^{36}O_2$ products in the $H_2^{16}O$ electrolyte, and further precise proportion of the $^{32}O_2$, $^{34}O_2$, and $^{36}O_2$ in the $H_2^{16}O$ electrolyte (Fig. 6c) reveals that $NiSe_2$-induced NiOOH has an almost negligible $^{36}O_2/^{32}O_2$ ratio, while the $^{34}O_2/^{32}O_2$ results are increased by ~320% compared to that of $Ni(OH)_2$ and NiTe-induced NiOOH. This result suggests that most of the volatilized O_2 in the $NiSe_2$-induced NiOOH samples is generated through the LOM scenario on the surface.

In brief, the operando Raman and DEMS successfully detected the catalytic intermediates and isotope-labeled products of NiOOH induced by the nickel-based precatalytic compounds. At this stage, we can basically recognize that the reconstructed active species oxy-hydroxides with sub-nanometric structural differences effectively regulate the frontier orbital energy levels, thus orienting to navigate the reconfiguration of active oxygen intermediates as well as the selective optimization of the dominant catalytic pathways of the OERs. In contrast, NiS_2-NiOOH follows the OPM pathway to produce oxygen with minimum energy consumption, and the catalytic activity was superior to the OER benchmark RuO_2. It still exhibits notable activity and kinetics compared to some previously reported transition metal-based electrocatalysts (Supplementary Table 26)[54,55], demonstrating stronger potential for practical application in water splitting and the pragmatic utility of designing catalytic materials via modulating the structural properties of reconstructed active units.

Alkaline water electrolysis device performance

To assess practical viability, we evaluated catalyst performance under industrial-grade alkaline conditions (30% KOH, 80 °C). $Ni(OH)_2$ and NiS_2 materials were scaled on nickel foam substrates (110 mm diameter electrodes) and integrated into the alkaline water electrolyser stack as anode materials (Electrode diameter 110 mm), paired with commercial Raney Nickel cathodes (Fig. 6d, e and Supplementary Fig. 65). The current density of the electrolyser stack composed of Raney Nickel (cathode) +NiS_2-NiOOH (anode) is much higher than that of the electrolyser stack composed of Raney Nickel (cathode) +$Ni(OH)_2$-NiOOH (anode) under the same cell voltage. At a current density of 250 mA cm^{-2}, the cell voltage is 1.681 V for Raney Nickel +NiS_2-NiOOH-based cell (Power consumption is 4.02 kWh Nm^3 H_2), which is much less than that of 1.886 V for Raney Nickel +$Ni(OH)_2$-NiOOH-based cell (Power consumption is 4.51 kWh Nm^3 H_2). The Raney Nickel +NiS_2-NiOOH-based electrolyser stack can be stably operated for at least 800 h at a larger current density of 250 mA cm^{-2}, indicating the high stability and potential for practical large-scale application of the catalytic materials.

Discussion

In summary, we find and quantitatively recognize the sub-nanometric fine-structural differences of the active unit NiO_6 with the tuned symmetry in confined nano-interfaces, which underlies the structural and chemical origin for the activity variance of the reconstructed oxyhydroxide structure from the nickel-based pre-catalysts. The geometric structure (bond length) and electronic structure (covalency) in the precatalytic material cooperatively account for the regular distortion of the NiO_6 active unit in the terminated structure NiOOH, based on which, the spatial-temporal multiple-induced mechanism has been further revealed. In comparison to $Ni(OH)_2$ and NiTe, NiOOH formed by NiS_2 and $NiSe_2$ reconstruction features larger structural distortions, which encourages the relative alteration of the p and d bands in the frontier orbitals, further facilitating the modulation of the catalytic intermediate configurations and the selective optimization of the shift from an AEM-dominated OER path to an OPM or LOM-dominated path. NiS_2-NiOOH exhibits enhanced catalytic activity with
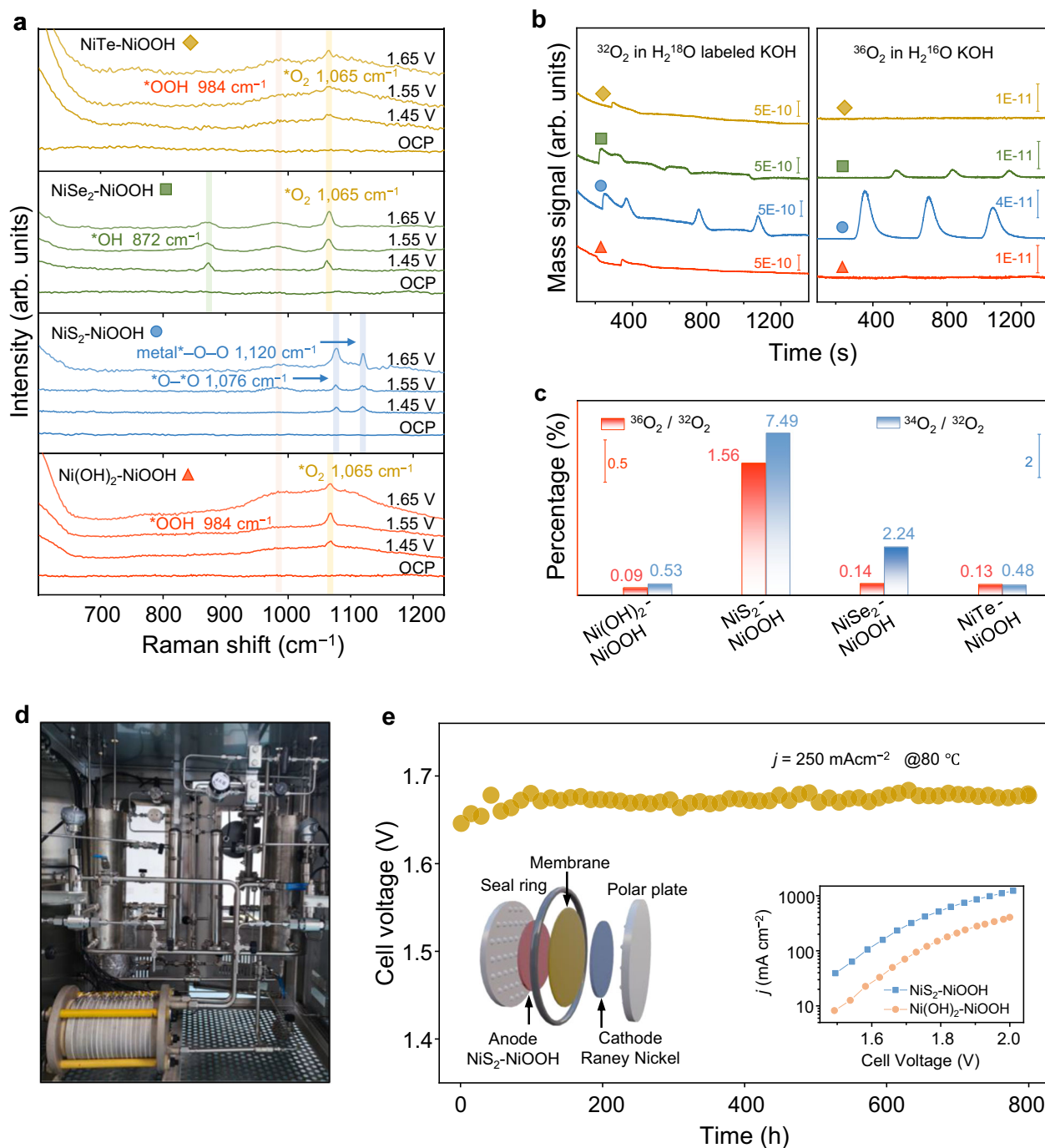
Fig. 6 | OER pathway verification and alkaline water electrolysis evaluation.
a Operando Raman spectra recorded at OCP, 1.45 V, 1.55 V, and 1.65 V (vs. RHE). The * symbol represents catalytic sites. **b** DEMS signals of O_2 products in the electrolyte using $H_2^{18}O$ (Left) and $H_2^{16}O$ (Right) as the solvent during three times of LSV in the potential range of 1.1–1.7 V versus RHE, with a 5 mV s^{-1} scan rate. **c** The ratio of the reaction products $^{32}O_2$, $^{34}O_2$, and $^{36}O_2$ from DEMS signals cycled in $H_2^{16}O$ aqueous KOH electrolyte. **d** Photograph of an industrial electrolyser device. **e** Stability tests of the Raney Nickel +NiS_2-NiOOH-based electrolyser stack. Insets are the schematic illustration of the structure of an electrolyser cell and the electrocatalytic water splitting performance of the Raney Nickel +NiS_2-NiOOH and the Raney Nickel +$Ni(OH)_2$-NiOOH measured in the industrial conditions. Source data are provided as a Source Data file.

overpotentials as low as 218 mV@10 mA cm^{-2} and the power consumption of the alkaline water electrolysis device is in the low range of 4.02 kWh Nm^3 H_2. This work deepens the understanding of the structure-activity correlation for the truly active phases from the perspective of configuration states and symmetry of active units at the sub-nanometer scale, intending to exemplify a demonstration for exploring potential future applications of efficient materials in the field of green energy.

Methods

Material synthesis

The Ni-based precatalytic compounds in our synthesized series were obtained by subsequent treatment of the precursor β-Ni(OH)$_2$ ultra-thin layered nanosheets. The β-Ni(OH)$_2$ layered nanosheets were first prepared by a hydrothermal method by weighing 2.4 mmol of nickel acetate (C$_4$H$_6$NiO$_4$·4H$_2$O, Aladdin, ≥99.9% purity) with a precision balance, 2.2 g of cetyltrimethylammonium bromide (CTAB, J&K, 99%

purity) were mixed and then dissolved in 60 mL of ethanol (Sinopharm Chemical Reagent Corp, ≥99.7%) and 11 mL of deionized water (resistance of 18 MΩ cm), which was magnetically stirred for 30 min to make the mixture homogeneous and used as the reaction precursor solution. Next, the growth solution was transferred to a 100 mL reaction kettle and then heated in a blast drying oven at 180 °C for 24 h. After natural cooling to room temperature, the β-Ni(OH)$_2$ layered nanosheet product could be obtained by ultrasonic cleaning and centrifugation with a large amount of deionized water, and the samples were removed and weighed after drying in a vacuum drying oven at 60 °C for subsequent use. Next, we prepared NiS$_2$, NiSe$_2$, and NiTe layered nanosheets by hydrothermal method, and the preparational details are shown in Supplementary Fig. 1. NiS$_2$ was synthesized through 10 mg Ni(OH)$_2$ with 300 mg Thioacetamide (TAA, CH$_3$CSNH$_2$, Sigma-Aldrich, 98.0%) and 35 mL deionized water in a 50 mL Teflon-lined stainless-steel autoclave at 180 °C for 12 h. NiSe$_2$ was prepared by 10 mg Ni(OH)$_2$ with 3.75 mmol Se powder (Aladdin, 99.9%), 7.5 mmol sodium hydroxide (NaOH, Aladdin, 96%) and 0.2 mL hydrazine hydrate (N$_2$H$_4$·H$_2$O, 50 wt.% content, J&K) in a 50 mL Teflon-lined stainless-steel autoclave filled with 30 mL N, N-Dimethylformamide (DMF, HCON(CH$_3$)$_2$, Aladdin, 99.9%) at 180 °C for 2 h. NiTe was obtained using 10 mg Ni(OH)$_2$ with 0.1 mmol Sodium tellurite (Na$_2$TeO$_3$, Alfa Aesar, 99.5%), 2.5 mL Ammonium hydroxide solution (NH$_3$·H$_2$O, Macklin, 25–28%), 0.5 mL hydrazine hydrate (N$_2$H$_4$·H$_2$O, 50 wt.% content, J&K) in a 50 mL Teflon-lined stainless-steel autoclave filled with 30 mL deionized water at 150 °C for 6 h.

Characterizations

Structural characterization of the catalysts was conducted using a Rigaku SmartLab 9 kW X-ray diffractometer (XRD, Cu-Kα, λ = 1.5418 Å) with 2θ ranging from 10° to 90° at 2° min^{-1}. Surface chemical states were analyzed by X-ray photoelectron spectroscopy (XPS) (Thermo Scientific ESCALab250) employing a monochromatic Al Kα source (150 W) under ultra-high vacuum (6.5×10^{-10} mbar), with narrow-spectrum scans collected at 30 eV pass energy. All binding energies were calibrated against adventitious carbon (C 1s = 284.8 eV). Microstructural features and elemental distribution were examined by transmission electron microscopy (TEM, JEM-120F) equipped with energy-dispersive X-ray spectroscopy (EDS, JEOL JED-2300) at 200 kV. Electron paramagnetic resonance (EPR) profiles were acquired on a Bruker EMXnano spectrometer. Trace element concentrations in OER electrolytes were quantified by the inductively coupled plasma-mass spectrometry (ICP-MS, Agilent 7800). Surface-sensitive Ni L-edge X-ray absorption spectroscopy (XAS) was conducted at the 4B7B beamline of Beijing Synchrotron Radiation Facility (BSRF) using total electron yield detection, with photon energy scanned from 840–880 eV in 0.1 eV increments.

Electrochemical measurements

Electrochemical assessments were conducted using a CHI 760 electrochemical workstation (Shanghai Chenhua) under ambient conditions. The three-electrode H-type cell comprised: (i) working electrode, catalyst-loaded carbon paper (TORAY, 0.18 mm) with 0.4 mg cm^{-2} loading, (ii) counter electrode, platinum foil (Tjaida), and (iii) reference electrode, Hg/HgO (1 M KOH, Tjaida). Electrode fabrication involved ultrasonic homogenization (1 h) of 4 mg nickel-based precursor in 1 mL aqueous-organic solvent blend (650 μL water, 330 μL alcohol) containing 20 μL Nafion (5%; Sigma-Aldrich), followed by controlled deposition of 50 μL ink onto 0.5 cm^2 carbon substrate. The H-type cell incorporated ZIRFON UTP 500+ membrane (3 cm diameter, 500 ± 50 μm thickness) pre-treated in 30% KOH (24 h activation). The KOH solution (pH=13.6 ± 0.2) was prepared within 30 min prior to the test by weighing 5.6 g of solid KOH (Aladdin, 99.999%, metals basis) and diluting to 100 mL with deionized water, followed by argon purging. Calibrate the Hg/HgO electrode by measuring its

potential against a standard Ag/AgCl reference (in saturated KCl) in Ar-saturated 1 M KOH. Stabilize the open-circuit potential for ≥1 h, calculate theoretical values via the Nernst equation, apply temperature corrections, and confirm reproducibility (±5 mV) across triplicate measurements. Polarization behavior was probed through cyclic voltammetry (CV) and linear sweep voltammetry (LSV) at 5 mV·s^{-1} scan rate in Ar-saturated 1 M KOH. Electrochemical impedance spectra were acquired in 100 kHz–10 mHz frequency domain with 10 mV a.c. perturbation at 1.5 V vs. RHE (η = 270 mV). The electrochemical double-layer capacitor (C_{dl}) determination employed cyclic voltammetry across 0.7–0.8 V vs. RHE window, where capacitive current differentials ($\Delta i/2 = |j_{anodic} − j_{cathodic}|/2$) exhibited linear correlation with scan rates, enabling C_{dl} calculation via regression analysis. A specific capacitance of 1 cm^2 flat surface area generally corresponds to 40 μF. Therefore, the electrochemical active specific surface area (ECSA) can be obtained from Eq. (1)[3,44].

$$ECSA = C_{dl}/0.04 \ (cm^2) \tag{1}$$

All potentials were calibrated versus the reversible hydrogen electrode (vs. RHE) using Eq. (2).

$$E(RHE) = E(Hg/HgO) + 0.098V + 0.0592 \times pH \tag{2}$$

For all polarization curves presented in the paper, the iR values were manually corrected with the series resistance (R_s) on the basis of the Eq. (3)[44].

$$E(RHE) = E(Hg/HgO) + 0.098V + 0.0592 \times pH − 0.95 \times iR_s \tag{3}$$

i is the current measured and there is compensation for 95% of the resistance R. The compensated ohmic R_s values were obtained from the fittings of the electrochemical impedance spectroscopy. The resistance values were 2.74 Ω for Ni(OH)$_2$-NiOOH, 1.61 Ω for NiS$_2$-NiOOH, 2.72 Ω for NiSe$_2$-NiOOH, 2.26 Ω for NiTe-NiOOH, 1.46 Ω for RuO$_2$ on carbon paper electrode.

Turnover frequency (TOF) calculation of the catalysts: The TOF values are calculated from the Eq. (4).

$$TOF = J \times A/(4 \times F \times n) \tag{4}$$

Where J is the current density at given overpotentials, A is the surface area of the electrode, F is the Faraday constant (a value of 96485 C mol^{-1}), and n is the number of moles of metal on the electrode[56]. Three independent measurements were made at least to obtain the standard deviation.

Operando Raman spectroscopy

Raman spectroscopy was conducted on a Horiba Jobin-Yvon Labram HR 800 system equipped with a diode-pumped solid-state laser (532 nm excitation wavelength, 250 mW). The incident laser power was attenuated by two orders of magnitude prior to sample irradiation. Spectral acquisition employed a 50× long-working-distance objective lens (8 mm focal length) with real-time monitoring via Labspec software, where energy calibration was routinely validated using a silicon standard (520.7 cm^{-1} characteristic peak). The operando electrochemical cell (Supplementary Fig. 66) incorporated a three-electrode configuration with Ag/AgCl reference and platinum wire counter electrodes, immersed in argon-saturated 1 M KOH electrolyte, as similarly reported previously of ref. 56. Working electrodes were prepared by depositing 10 μL of catalyst ink onto 3 mm silver electrode, where the ink formulation consisted of 2 mg catalyst powder homogenized with 20 μL Nafion solution (5 wt%) in 1 mL water/ethanol mixed solvent (vol/vol = 3:1) through 30-min ultrasonic processing.

Steady-state spectra collection commenced after maintaining the applied potentials for 5 min to establish equilibrium conditions.

Operando X-ray absorption measurements

Synchrotron-based X-ray absorption fine structure measurements of Ni K-edge spectra were conducted at two beamlines: Ni-based pre-catalytic compounds acquired at the 1W2B beamline at the Beijing Synchrotron Radiation Facility (BSRF) using powder samples, while operando studies utilized the BL20U1 beamline at the Shanghai Synchrotron Radiation Facility (SSRF) with a custom electrochemical cell (Supplementary Fig. 66). The catalysts were sprayed onto carbon paper with Kapton film encapsulation on the back as working electrodes ($1 \times 1\,cm^2$ active area), ensuring full electrolyte contact in 1 M KOH. Fluorescence-mode data collection tracked dynamic structural evolution during OER, with applied potentials stepped from open-circuit condition to 1.15, 1.35, 1.45, and 1.55 vs. RHE (2 h equilibration per step). Energy calibration established the absorption edge position ($E0$, 8333.00 eV) using metallic Ni foil as reference, with all spectra acquired during one period of beam time. Ni foil and Ni_2O_3 standards (Macklin, 99.5%) were measured in the transmission mode. The $E0$ position was determined from the maximum derivative of XANES spectra. Data processing involved sequential steps in Athena 0.9.25: pre-edge background subtraction and post-edge normalization. Subsequent Fourier transform analysis in Artemis 0.9.25 applied the EXAFS equation:

$$\chi(k) = S_0^2 \sum_j \frac{CN_j F_j(k)}{kR_j^2} \exp\left[-2k^2\sigma_j^2\right] e^{-2R_j/\lambda_j(k)} \sin\left[2kR_j + \phi_j(k)\right],$$

where CN_j (coordination number), R_j (interatomic distance), and σ_j^2 (Debye-Waller factor) were freely refined parameters. S_0^2 stands for the amplitude decay factor. $F_j(k)$ is the initial amplitude function of the shell layer j, and $\lambda_j(k)$ is the mean free path of the electrons. The sinusoidal term $\sin[2kR_j + \varphi_j(k)]$ reflects the oscillations in the EXAFS spectrum. Fitting employed k^3-weighting within $3-12\,Å^{-1}$ k-space, with R-space analysis limited to 1–3 Å. Theoretical scattering paths were generated for Ni, $Ni(OH)_2$, NiS_2, $NiSe_2$, $NiTe$, and NiOOH structural models. All four parameters (CN, R, σ^2, $\Delta E0$) underwent unconstrained fitting without inter-parameter correlations or fixed values, ensuring physically meaningful results[39,40,56].

Operando X-ray diffraction measurements

X-ray diffraction was performed using a Rigaku SmartLab 9 kW instrument (Cu target, 45 kV, 200 mA). Specific operando XRD measurements were carried out in a homemade cell filled with 1 M KOH electrolyte with Ag/AgCl and platinum wire as reference and counter electrodes, respectively (Supplementary Fig. 66). The spectra were collected after holding the studied samples at the desired potentials (OCP, 1.15 V, 1.35 V, 1.45 V, 1.55 V and 1.65 V vs. RHE) for 2 h. To prepare the working electrode, 5 mg of electrocatalyst and 20 µL of Nafion solution (5 wt%, Sigma-Aldrich) were ultrasonically dispersed in 1 mL of water/ethanol (v/v ratio = 3:1) solution to form a homogeneous ink. The electrocatalyst suspension (50 µL) was applied on a glass-carbon electrode (8 mm) as the working electrode.

Operando differential electrochemical mass spectroscopy measurements

Operando ^{18}O-labeled isotope tracking was achieved using a QAS100 differential electrochemical mass spectrometer (DEMS, Linglu Instruments) coupled to a dual-chamber vacuum system (Supplementary Fig. 66), similarly to the system reported by Lin et al.[3]. The configuration integrates a high-vacuum mass analysis chamber (10^{-7} mbar) with a mild-vacuum interface connected to an ambient-pressure electrochemical cell, leveraging pressure gradients to continuously extract gaseous products for real-time analysis. Working electrodes were fabricated by magnetron-sputtering Au onto 50 µm porous PTFE membranes (Linglu, porosity: ≥50%, pore size: ≤20 nm), followed by catalyst deposition via drop-casting. The hydrophobic PTFE/Au architecture enabled selective gas transport to the analyzer while preventing electrolyte penetration. A Pt wire counter electrode and Ag/AgCl reference completed the three-electrode setup in Ar-purged 1 M KOH. Surface ^{18}O labeling of the reconstructed materials involved cyclic polarization (1.1 V–1.7 V vs. RHE, 5 mV s^{-1}) in ^{18}O-enriched KOH electrolyte using ^{18}O isotope-labeled water (97 atom% of ^{18}O, J&K) for three cycles, during which the mass signals of the gaseous products $^{32}O_2$, $^{34}O_2$ and $^{36}O_2$ were continuously monitored. Subsequent thorough rinsing with abundant $H_2^{16}O$ removed physisorbed ^{18}O species while retaining chemically bonded oxygen. Operando tracking then proceeded in natural 1 M KOH with $H_2^{16}O$ as the solvent, correlating applied potentials with mass/charge signals (m/z = 32, 34, 36) to elucidate oxygen evolution pathways.

DFT calculations

First-principles calculations incorporating spin polarization were conducted using the Vienna Ab initio Simulation Package (VASP) with the projector augmented wave (PAW) method[57,58]. The exchange-correlation functional was treated within the generalized gradient approximation (GGA-PBE)[59], supplemented by a Hubbard U correction (U = 5.5 eV) applied to Ni 3d orbitals[41]. A plane-wave energy cutoff of 450 eV and Gaussian smearing (0.2 eV width) were employed for Kohn-Sham orbital occupation. The bulk structure of NiOOH (8 Ni atoms in one bulk) was optimized, where the Monkhorst mesh of $4 \times 4 \times 2$ was used. The optimized lattice parameter was obtained through the method, fitting by the equation of state (EOS). Note that, the lattice of the a and b axis of the bulk structures were optimized by EOS, and the c axis was optimized automatically. In the EOS fitting, the total energies of the bulk were calculated with different lattice parameters of a = b = 5.60, 5.70, 5.75, 5.80, 5.85, 5.90, and 6.00 Å. The optimized lattice parameter can be obtained at the minimum by fitting the total energy with the lattice parameter as a quadratic polynomial, which was calculated as 5.82 Å (For details see Supplementary Data1). The tensile strain for the structures was conducted by modifying the optimized lattice parameter (5.82 Å) artificially, where the tensile strain of 0.5%, 1.0%, 1.5%, and 2.0% were considered. The NiOOH (10 − 1) surface[43,46] was built with 4 Ni layers (32 Ni atoms in total) with all the calculations on the surfaces following the Monkhorst mesh of $2 \times 2 \times 1$, where the stretched surface was established based on the stretched bulk structures. The oxygen vacancies were considered on the surface, where the lattice parameter of the surface was fixed in all the surface calculations. Convergence criteria included energy thresholds of 10^{-5} eV and force tolerances below 0.05 eV/Å.

Electrochemical step energetics were evaluated employing the computational hydrogen electrode (CHE) methodology[60], with free energy corrections systematically incorporated at 298 K. The total Gibbs free energy is expressed as:

$$\Delta G = \Delta E + \Delta G_{ZPE} + \Delta G_U - T\Delta S$$

where ΔE denotes the DFT-derived electronic energy difference, ΔG_{ZPE} the zero-point vibrational correction, ΔG_U the thermal internal energy contribution, and ΔS the entropic term at 298 K[61]. Solvent stabilization effects were incorporated through empirical corrections of −0.17 eV (*OH) and −0.20 eV (*OOH), accounting for hydrogen-bond stabilization within the aqueous solvation environment[62].

Data availability

The data generated in this study are provided in the Supplementary Information/Source Data file. Source data are provided with this paper.

References

1. Hwang, J. et al. Perovskites in catalysis and electrocatalysis. *Science* **358**, 751–756 (2017).
2. Chong, L. et al. La- and Mn-doped cobalt spinel oxygen evolution catalyst for proton exchange membrane electrolysis. *Science* **380**, 609–616 (2023).
3. Lin, C. et al. In-situ reconstructed Ru atom array on α-MnO$_2$ with enhanced performance for acidic water oxidation. *Nat. Catal.* **4**, 1012–1023 (2021).
4. Wang, Z., Goddard, W. A. & Xiao, H. Potential-dependent transition of reaction mechanisms for oxygen evolution on layered double hydroxides. *Nat. Commun.* **14**, 4228 (2023).
5. Zhong, H. et al. Optimization of oxygen evolution activity by tuning e_g* band broadening in nickel oxyhydroxide. *Energy Environ. Sci.* **16**, 641–652 (2023).
6. Bergmann, A. et al. Unified structural motifs of the catalytically active state of Co(oxyhydr)oxides during the electrochemical oxygen evolution reaction. *Nat. Catal.* **1**, 711–719 (2018).
7. Sun, Y. et al. Covalency competition dominates the water oxidation structure-activity relationship on spinel oxides. *Nat. Catal.* **3**, 554–563 (2020).
8. Cho, J. et al. Importance of broken geometric symmetry of single-atom Pt sites for efficient electrocatalysis. *Nat. Commun.* **14**, 3233 (2023).
9. Seh, Z. W. et al. Combining theory and experiment in electrocatalysis: Insights into materials design. *Science* **355**, 1 (2017).
10. Zheng, X. et al. Theory-driven design of high-valence metal sites for water oxidation confirmed using in situ soft X-ray absorption. *Nat. Chem.* **10**, 149–154 (2018).
11. Net zero by 2050: A roadmap for the global energy sector (*International Energy Agency*, 2021).
12. Suntivich, J., May, K. J., Gasteiger, H. A., Goodenough, J. B. & Shao-Horn, Y. A perovskite oxide optimized for oxygen evolution catalysis from molecular orbital principles. *Science* **334**, 1383–1385 (2011).
13. Wang, X. et al. Pivotal role of reversible NiO$_6$ geometric conversion in oxygen evolution. *Nature* **611**, 702–708 (2022).
14. Zhou, Y. et al. Enlarged Co–O covalency in octahedral sites leading to highly efficient spinel oxides for oxygen evolution reaction. *Adv. Mater.* **30**, 1802912 (2018).
15. Song, J. et al. A review on fundamentals for designing oxygen evolution electrocatalysts. *Chem. Soc. Rev.* **49**, 2196–2214 (2020).
16. Lei, X. et al. High-entropy single-atom activated carbon catalysts for sustainable oxygen electrocatalysis. *Nat. Sustain.* **6**, 816–826 (2023).
17. Li, H., Zhao, J., Luo, L., Du, J. & Zeng, J. Symmetry-breaking sites for activating linear carbon dioxide molecules. *Acc. Chem. Res.* **54**, 1454–1464 (2021).
18. Hong, W. T. et al. Charge-transfer-energy-dependent oxygen evolution reaction mechanisms for perovskite oxides. *Energy Environ. Sci.* **10**, 2190–2200 (2017).
19. Assat, G. & Tarascon, J.-M. Fundamental understanding and practical challenges of anionic redox activity in Li-ion batteries. *Nat. Energy* **3**, 373–386 (2018).
20. Zhong, H. et al. Fundamental understanding of structural reconstruction behaviors in oxygen evolution reaction electrocatalysts. *Adv. Energy Mater.* **13**, 2301391 (2023).
21. Khorshidi, A., Violet, J., Hashemi, J. & Peterson, A. A. How strain can break the scaling relations of catalysis. *Nat. Catal.* **1**, 263–268 (2018).
22. Liu, H. et al. Construction of asymmetrical dual Jahn-Teller sites for photocatalytic CO$_2$ reduction. *Angew. Chem. Int. Ed.* **62**, e202304562 (2023).
23. Huang, Z.-F. et al. Chemical and structural origin of lattice oxygen oxidation in Co–Zn oxyhydroxide oxygen evolution electrocatalysts. *Nat. Energy* **4**, 329–338 (2019).
24. Petrie, J. R. et al. Enhanced bifunctional oxygen catalysis in strained LaNiO$_3$ perovskites. *J. Am. Chem. Soc.* **138**, 2488–2491 (2016).
25. Chen, Y. et al. Enhanced oxygen evolution over dual corner-shared cobalt tetrahedra. *Nat. Commun.* **13**, 5510 (2022).
26. Zhou, G. et al. Spin-related symmetry breaking induced by half-disordered hybridization in Bi$_x$Er$_{2-x}$Ru$_2$O$_7$ pyrochlores for acidic oxygen evolution. *Nat. Commun.* **13**, 4106 (2022).
27. Zhao, S. et al. Structural transformation of highly active metal–organic framework electrocatalysts during the oxygen evolution reaction. *Nat. Energy* **5**, 881–890 (2020).
28. Dionigi, F. et al. In-situ structure and catalytic mechanism of NiFe and CoFe layered double hydroxides during oxygen evolution. *Nat. Commun.* **11**, 2522 (2020).
29. Liu, L. & Corma, A. Structural transformations of solid electrocatalysts and photocatalysts. *Nat. Rev. Chem.* **5**, 256–276 (2021).
30. Monai, M. et al. Restructuring of titanium oxide overlayers over nickel nanoparticles during catalysis. *Science* **380**, 644–651 (2023).
31. Martín, A. J., Mitchell, S., Mondelli, C., Jaydev, S. & Pérez-Ramírez, J. Unifying views on catalyst deactivation. *Nat. Catal.* **5**, 854–866 (2022).
32. Yuan, W. T. et al. In situ manipulation of the active Au-TiO$_2$ interface with atomic precision during CO oxidation. *Science* **371**, 517–521 (2021).
33. Mefford, J. T. et al. Correlative operando microscopy of oxygen evolution electrocatalysts. *Nature* **593**, 67–73 (2021).
34. Chen, J. Y. C. et al. Operando Analysis of NiFe and Fe Oxyhydroxide Electrocatalysts for Water Oxidation: Detection of Fe4+ by Mössbauer Spectroscopy. *J. Am. Chem. Soc.* **137**, 15090–15093 (2015).
35. Hu, Y. et al. Understanding the sulphur-oxygen exchange process of metal sulphides prior to oxygen evolution reaction. *Nat. Commun.* **14**, 1949 (2023).
36. Huang, J. et al. Identification of key reversible intermediates in self-reconstructed nickel-based hybrid electrocatalysts for oxygen evolution. *Angew. Chem. Int. Ed.* **58**, 17458–17464 (2019).
37. Li, S. et al. Coordination environment tuning of nickel sites by oxyanions to optimize methanol electro-oxidation activity. *Nat. Commun.* **13**, 2916 (2022).
38. Luo, R. et al. Re-looking into the active moieties of metal X-ides (X- = Phosph-, Sulf-, Nitr-, and Carb-) toward oxygen evolution reaction. *Adv. Funct. Mater.* **31**, 2102918 (2021).
39. Arcon, I., Mirtic, B. & Kodre, A. Determination of valence states of chromium in calcium chromates by using X-ray absorption near-edge structure (XANES) spectroscopy. *J. Am. Ceram. Soc.* **81**, 222–224 (1998).
40. Newville, M. IFEFFIT: interactive XAFS analysis and FEFF fitting. *J. synchrotron Radiat.* **8**, 322–324 (2001).
41. Kang, J. et al. Valence oscillation and dynamic active sites in monolayer NiCo hydroxides for water oxidation. *Nat. Catal.* **4**, 1050–1058 (2021).
42. Sun, Y. et al. A site management prompts the dynamic reconstructed active phase of perovskite oxide OER catalysts. *Adv. Energy Mater.* **11**, 2003755 (2021).
43. Zhang, N. et al. Lattice oxygen activation enabled by high-valence metal sites for enhanced water oxidation. *Nat. Commun.* **11**, 4066 (2020).
44. Wei, C. et al. Recommended practices and benchmark activity for hydrogen and oxygen electrocatalysis in water splitting and fuel cells. *Adv. Mater.* **31**, 1806296 (2019).
45. Vrubel, H., Moehl, T., Grätzel, M. & Hu, X. Revealing and accelerating slow electron transport in amorphous molybdenum sulphide particles for hydrogen evolution reaction. *Chem. Commun.* **49**, 8985–8987 (2013).
46. Bajdich, M., García-Mota, M., Vojvodic, A., Nørskov, J. K. & Bell, A. T. Theoretical investigation of the activity of cobalt oxides for the

electrochemical oxidation of water. *J. Am. Chem. Soc.* **135**, 13521–13530 (2013).

47. Wang, N. et al. Doping shortens the metal/metal distance and promotes oh coverage in non-noble acidic oxygen evolution reaction catalysts. *J. Am. Chem. Soc.* **145**, 7829–7836 (2023).

48. Huang, Z.-F. et al. Tuning of lattice oxygen reactivity and scaling relation to construct better oxygen evolution electrocatalyst. *Nat. Commun.* **12**, 3992 (2021).

49. Lang, C. et al. Observation of a potential-dependent switch of water-oxidation mechanism on Co-oxide-based catalysts. *Chem* **7**, 2101–2117 (2021).

50. Cheng, W. et al. Lattice-strained metal-organic-framework arrays for bifunctional oxygen electrocatalysis. *Nat. Energy* **4**, 115–122 (2019).

51. Wang, B. et al. In situ structural evolution of the multi-site alloy electrocatalyst to manipulate the intermediate for enhanced water oxidation reaction. *Energy Environ. Sci.* **13**, 2200–2208 (2020).

52. Zhang, J. et al. Strong metal-support interaction boosts activity, selectivity, and stability in electrosynthesis of H_2O_2. *J. Am. Chem. Soc.* **144**, 2255–2263 (2022).

53. Wen, Y. et al. Stabilizing highly active Ru sites by suppressing lattice oxygen participation in acidic water oxidation. *J. Am. Chem. Soc.* **143**, 6482–6490 (2021).

54. Wang, S. et al. High valence state of Ni and Mo synergism in NiS_2-MoS_2 hetero-nanorods catalyst with layered surface structure for urea electrocatalysis. *J. Energy Chem.* **66**, 483–492 (2022).

55. Yin, C., Yang, F., Wang, S. & Feng, L. Heterostructured $NiSe_2$/$MoSe_2$ electronic modulation for efficient electrocatalysis in urea assisted water splitting reaction. *Chin. J. Catal.* **51**, 225–236 (2023).

56. Sun, Y. et al. Phase reconfiguration of multivalent nickel sulfides in hydrogen evolution. *Energy Environ. Sci.* **15**, 633–644 (2022).

57. Kresse, G. & Furthmüller, J. Efficiency of ab-initio total energy calculations for metals and semiconductors using a plane-wave basis set. *Comp. Mater. Sci.* **6**, 15–50 (1996).

58. Blochl, P. E. Projector augmented-wave method. *Phys. Rev. B Condens. Matter* **50**, 17953–17979 (1994).

59. Perdew, J. P. et al. Atoms, molecules, solids, and surfaces: Applications of the generalized gradient approximation for exchange and correlation. *Phys. Rev. B Condens. Matter* **46**, 6671–6687 (1992).

60. Nørskov, J. K. et al. Origin of the Overpotential for Oxygen Reduction at a Fuel-Cell Cathode. *J. Phys. Chem. B* **108**, 17886–17892 (2004).

61. Guo, C. et al. Computational Design of Spinel Oxides through Coverage-Dependent Screening on the Reaction Phase Diagram. *ACS Catal.* **12**, 6781–6793 (2022).

62. Guo, C., Fu, X. & Xiao, J. Theoretical Insights on the Synergy and Competition between Thermochemical and Electrochemical Steps in Oxygen Electroreduction. *J. Phys. Chem. C.* **124**, 25796–25804 (2020).

Acknowledgements

Author contributions

Z.K. and Y.Z. designed and proposed the research direction, initiated and supervised the project. Y.S. performed the experiments. Y.X., J.W. and Y.S. carried out the DFT simulations. Y.S. and X.C. designed and analyzed the operando Raman and XAFS measurements. P.L., X.W. and Z.T. assisted with XAFS experiments and discussions about DFT simulations. Z.T. and Z.J. contributed to the analysis of electrochemical performance. Z.J. and W.Z. assisted in carrying out the XRD, SEM, XPS, TEM and EDS measurements. All the authors discussed the results and participated in writing the manuscript.

Competing interests

The authors declare no competing interests.

Additional information

Supplementary information The online version contains supplementary material available at https://doi.org/10.1038/s41467-025-58424-y.

Correspondence and requests for materials should be addressed to Zhuo Kang or Yue Zhang.

Peer review information *Nature Communications* thanks Ligang Feng and the other anonymous reviewer(s) for their contribution to the peer review of this work. A peer review file is available

Reprints and permissions information is available at http://www.nature.com/reprints

Publisher's note Springer Nature remains neutral with regard to jurisdictional claims in published maps and institutional affiliations.